

# Pre-clinical longitudinal monitoring of hemodynamic response to anti-vascular chemotherapy by hybrid diffuse optics

PARISA FARZAM,<sup>1,2</sup> JOHANNES JOHANSSON,<sup>1,3</sup> MIGUEL MIRELES,<sup>1</sup>  
GABRIELA JIMÉNEZ-VALERIO,<sup>4</sup> MAR MARTÍNEZ-LOZANO,<sup>4</sup> REGINE  
CHOE,<sup>5,6</sup> ORIOL CASANOVAS,<sup>4</sup> AND TURGUT DURDURAN<sup>1,7,\*</sup>

<sup>1</sup>ICFO-Institut de Ciències Fotòniques, The Barcelona Institute of Sciences and Technology, 08860, Castelldefels (Barcelona), Spain

<sup>2</sup>Athinoula A. Martinos Center for Biomedical Imaging, Massachusetts General Hospital, Harvard Medical School, Boston, MA 02129, USA

<sup>3</sup>Department of Biomedical Engineering, Linköping University, 58185 Linköping, Sweden

<sup>4</sup>Program Against Cancer Therapeutic Resistance (ProCURE), Catalan Institute of Oncology, Bellvitge Biomedical Research Institute – IDIBELL, 08908, L'Hospitalet de Llobregat (Barcelona), Spain

<sup>5</sup>Department of Biomedical Engineering, University of Rochester, Rochester, NY 14627, USA

<sup>6</sup>Department of Electrical and Computer Engineering, University of Rochester, Rochester, NY 14627, USA

<sup>7</sup>Institució Catalana de Recerca i Estudis Avançats (ICREA), 08015, Barcelona, Spain

\* [turgut.durduran@icfo.es](mailto:turgut.durduran@icfo.es)

**Abstract:** The longitudinal effect of an anti-vascular endothelial growth factor receptor 2 (VEGFR-2) antibody (DC 101) therapy on a xenografted renal cell carcinoma (RCC) mouse model was monitored using hybrid diffuse optics. Two groups of immunosuppressed male nude mice (seven treated, seven controls) were measured. Tumor microvascular blood flow, total hemoglobin concentration and blood oxygenation were investigated as potential biomarkers for the monitoring of the effect of therapy twice a week and were related to the final treatment outcome. These hemodynamic biomarkers have shown a clear differentiation between two groups by day four. Moreover, we have observed that pre-treatment values and early changes in hemodynamics are highly correlated with the therapeutic outcome demonstrating the potential of diffuse optics to predict the therapy response at an early time point.

© 2017 Optical Society of America

**OCIS codes:** (300.6480) Spectroscopy, speckle; (170.3890) Medical optics instrumentation; (170.1470) Blood or tissue constituent monitoring; (170.3660) Light propagation in tissues; (170.6510) Spectroscopy, tissue diagnostics; (110.4234) Multispectral and hyperspectral imaging.

## References and links

1. J. Folkman, "What is the evidence that tumors are angiogenesis dependent?" *J. Natl. Cancer Inst.* **82**(1), 4–6 (1990).
2. J. Folkman, "Angiogenesis in cancer, vascular, rheumatoid and other disease," *Nat. Med.* **1**(1), 27–30 (1995).
3. P. Carmeliet and R. K. Jain, "Angiogenesis in cancer and other diseases," *Nature* **407**(6801), 249–257 (2000).
4. N. Ferrara, H.-P. Gerber, and J. LeCouter, "The biology of VEGF and its receptors," *Nat. Med.* **9**(6), 669–676 (2003).
5. J. Folkman, "Angiogenesis: an organizing principle for drug discovery?" *Nat. Rev. Drug Discov.* **6**(4), 273–286 (2007).
6. L. M. Ellis and D. J. Hicklin, "VEGF-targeted therapy: mechanisms of anti-tumour activity," *Nat. Rev. Cancer* **8**(8), 579–591 (2008).
7. L. Moserle, G. Jiménez-Valerio, and O. Casanovas, "Antiangiogenic therapies: going beyond their limits," *Cancer Discov.* **4**(1), 31–41 (2014).
8. L. Hlatky, P. Hahnfeldt, and J. Folkman, "Clinical application of antiangiogenic therapy: microvessel density, what it does and doesn't tell us," *J. Natl. Cancer Inst.* **94**(12), 883–893 (2002).
9. C. Fontanella, E. Ongaro, S. Bolzonello, M. Guardascione, G. Fasola, and G. Aprile, "Clinical advances in the development of novel VEGFR2 inhibitors," *Ann. Transl. Med.* **2**(12), 123 (2014).
10. C. Coppin, C. Kollmannsberger, L. Le, F. Porzolt, and T. J. Wilt, "Targeted therapy for advanced renal cell cancer (RCC): a Cochrane systematic review of published randomised trials," *BJU Int.* **108**(10), 1556–1563 (2011).

11. I. Duran, J. Lambea, P. Maroto, J. L. González-Larriba, L. Flores, S. Granados-Principal, M. Graupera, B. Sáez, A. Vivancos, and O. Casanovas, "Resistance to Targeted Therapies in Renal Cancer: The Importance of Changing the Mechanism of Action," *Target. Oncol.* **12**, 19–35 (2016).
12. R. S. Kerbel, J. Yu, J. Tran, S. Man, A. Vilorio-Petit, G. Klement, B. L. Coomber, and J. Rak, "Possible mechanisms of acquired resistance to anti-angiogenic drugs: Implications for the use of combination therapy approaches," *Cancer Metastasis Rev.* **20**(1), 79–86 (2001).
13. H. P. Eikesdal and R. Kalluri, "Drug resistance associated with antiangiogenesis therapy," *Semin. Cancer Biol.* **19**(5), 310–317 (2009).
14. G. Bergers and D. Hanahan, "Modes of resistance to anti-angiogenic therapy," *Nat. Rev. Cancer* **8**(8), 592–603 (2008).
15. G. Klement, S. Baruchel, J. Rak, S. Man, K. Clark, D. J. Hicklin, P. Bohlen, and R. S. Kerbel, "Continuous low-dose therapy with vinblastine and VEGF receptor-2 antibody induces sustained tumor regression without overt toxicity," *The J. Clin. Invest.* **105**(8), R15–R24 (2000).
16. M. Braunagel, A. Graser, M. Reiser, and M. Notohamprodjjo, "The role of functional imaging in the era of targeted therapy of renal cell carcinoma," *World J. Urol.* **32**(1), 47–58 (2014).
17. H. B. Stone, J. M. Brown, T. L. Phillips, and R. M. Sutherland, "Oxygen in human tumors: correlations between methods of measurement and response to therapy. Summary of a workshop held November 19-20, 1992, at the National Cancer Institute, Bethesda, Maryland," *Radiat. Res.* **136**(3), 422–434 (1993).
18. P. Vaupel and A. Mayer, "Hypoxia in cancer: significance and impact on clinical outcome," *Cancer Metastasis Rev.* **26**(2), 225–239 (2007).
19. J. Allen and K. Howell, "Microvascular imaging: techniques and opportunities for clinical physiological measurements," *Physiol. Meas.* **35**(7), R91–R141 (2014).
20. M. S. Gee, H. M. Saunders, J. C. Lee, J. F. Sanzo, W. T. Jenkins, S. M. Evans, G. Trinchieri, C. M. Sehgal, M. D. Feldman, and W. M. Lee, "Doppler ultrasound imaging detects changes in tumor perfusion during antivascular therapy associated with vascular anatomic alterations," *Cancer Res.* **61**(7), 2974–2982 (2001).
21. D. E. Goertz, J. L. Yu, R. S. Kerbel, P. N. Burns, and F. S. Foster, "High-frequency Doppler ultrasound monitors the effects of antivascular therapy on tumor blood flow," *Cancer Res.* **62**(22), 6371–6375 (2002).
22. M. Tanter and M. Fink, "Ultrafast imaging in biomedical ultrasound," *IEEE Trans. Ultrason., Ferroelect., Freq. Control* **61**(1), 102–119 (2014).
23. C. Errico, B. F. Osmanski, S. Pezet, O. Couture, Z. Lenkei, and M. Tanter, "Transcranial functional ultrasound imaging of the brain using microbubble-enhanced ultrasensitive Doppler," *NeuroImage* **124**, 752–761 (2016).
24. B. J. Vakoc, D. Fukumura, R. K. Jain, and B. E. Bouma, "Cancer imaging by optical coherence tomography: preclinical progress and clinical potential," *Nat. Rev. Cancer* **12**(5), 363–368 (2012).
25. M. Draijer, E. Hondebrink, T. van Leeuwen, and W. Steenbergen, "Review of laser speckle contrast techniques for visualizing tissue perfusion," *Lasers Med. Sci.* **24**(4), 639–651 (2009).
26. J. D. Briers, "Laser Doppler, speckle and related techniques for blood perfusion mapping and imaging," *Physiol. Meas.* **22**(4), R35–R66 (2001).
27. F. Martelli, T. Binzoni, A. Pifferi, L. Spinelli, A. Farina, and A. Torricelli, "There's plenty of light at the bottom: statistics of photon penetration depth in random media," *Sci. Rep.* **6**(1), 27057 (2016).
28. R. Choe and T. Durduran, "Diffuse Optical Monitoring of the Neoadjuvant Breast Cancer Therapy," **18**(4), 1367–1386 (2012).
29. B. J. Tromberg, A. Cerussi, N. Shah, M. Compton, A. Durkin, D. Hsiang, J. Butler, and R. Mehta, "Imaging in breast cancer: diffuse optics in breast cancer: detecting tumors in pre-menopausal women and monitoring neoadjuvant chemotherapy," *Breast Cancer Res.* **7**(6), 279–285 (2005).
30. A. Cerussi, D. Hsiang, N. Shah, R. Mehta, A. Durkin, J. Butler, and B. J. Tromberg, "Predicting response to breast cancer neoadjuvant chemotherapy using diffuse optical spectroscopy," *Proc. Natl. Acad. Sci. U.S.A.* **104**(10), 4014–409 (2007).
31. C. Zhou, R. Choe, N. Shah, T. Durduran, G. Yu, A. Durkin, D. Hsiang, R. Mehta, J. Butler, A. Cerussi, B. J. Tromberg, and A. G. Yodh, "Diffuse optical monitoring of blood flow and oxygenation in human breast cancer during early stages of neoadjuvant chemotherapy," *J. Biomed. Opt.* **12**(5), 051903 (2007).
32. U. Sunar, H. Quon, T. Durduran, J. Zhang, J. Du, C. Zhou, G. Yu, R. Choe, A. Kilger, R. Lustig, L. Loevner, S. Nioka, B. Chance, and A. G. Yodh, "Noninvasive diffuse optical measurement of blood flow and blood oxygenation for monitoring radiation therapy in patients with Head Neck tumors: a pilot study," *J. Biomed. Opt.* **11**(6), 064021 (2006).
33. D. Roblyer, S. Ueda, A. Cerussi, W. Tanamai, A. Durkin, R. Mehta, D. Hsiang, J. a. Butler, C. McLaren, W.-P. Chen, and B. Tromberg, "Optical imaging of breast cancer oxyhemoglobin flare correlates with neoadjuvant chemotherapy response one day after starting treatment," *Proc. Natl. Acad. Sci. U.S.A.* **108**(35), 14626–14631 (2011).
34. S. Ueda, D. Roblyer, A. Cerussi, A. Durkin, A. Leproux, Y. Santoro, S. Xu, T. D. O'Sullivan, D. Hsiang, R. Mehta, J. Butler, and B. J. Tromberg, "Baseline tumor oxygen saturation correlates with a pathologic complete response in breast cancer patients undergoing neoadjuvant chemotherapy," *Cancer Res.* **72**(17), 4318–4328 (2012).
35. D. R. Busch, R. Choe, T. Durduran, and A. G. Yodh, "Towards non-invasive characterization of breast cancer and cancer metabolism with diffuse optics," *PET clinics* **8**(3), 345–365 (2013).
36. D. R. Busch, R. Choe, M. a. Rosen, W. Guo, T. Durduran, M. D. Feldman, C. Mies, B. J. Czerniecki, J. Tchou,

- A. Demichele, M. D. Schnall, and A. G. Yodh, "Optical malignancy parameters for monitoring progression of breast cancer neoadjuvant chemotherapy," *Biomedical Opt. Express* **4**(1), 105–21 (2013).
37. T. L. Becker, A. D. Paquette, K. R. Keymel, B. W. Henderson, and U. Sunar, "Monitoring blood flow responses during topical ALA-PDT," *Biomedical Opt. Express* **2**(1), 123–30 (2010).
38. S. H. Chung, M. D. Feldman, D. Martinez, H. Kim, M. E. Putt, D. R. Busch, J. Tchou, B. J. Czerniecki, M. D. Schnall, M. A. Rosen, A. DeMichele, A. G. Yodh, and R. Choe, "Macroscopic optical physiological parameters correlate with microscopic proliferation and vessel area breast cancer signatures," *Breast Cancer Res. : BCR* **17**(1), 72 (2015).
39. V. R. Kondepati, H. M. Heise, and J. Backhaus, "Recent applications of near-infrared spectroscopy in cancer diagnosis and therapy," *Anal. Bioanal. Chem.* **390**(1), 125 (2007).
40. C. Sessa, A. Guibal, G. Del Conte, and C. Rüegg, "Biomarkers of angiogenesis for the development of antiangiogenic therapies in oncology: tools or decorations?" *Nat. Clin. Pract. Oncol.* **5**(7), 378–391 (2008).
41. R. K. Jain, D. G. Duda, C. G. Willett, D. V. Sahani, A. X. Zhu, J. S. Loeffler, T. T. Batchelor, and A. G. Sorensen, "Biomarkers of response and resistance to antiangiogenic therapy," *Nat. Rev. Clin. Oncol.* **6**(6), 327–338 (2009).
42. W. K. Rathmell, T. M. Wright, and B. I. Rini, "Molecularly targeted therapy in renal cell carcinoma," *Expert Rev. Anticancer Ther.* **5**(6), 1031–1040 (2005).
43. J. a. Sosman, I. Puzanov, and M. B. Atkins, "Opportunities and obstacles to combination targeted therapy in renal cell cancer," *Clin. Cancer Res.* **13**(2 Pt 2), 764s–769s (2007).
44. L. Witte, D. J. Hicklin, Z. Zhu, B. Pytowski, H. Kotanides, P. Rockwell, and P. Böhlen, "Monoclonal antibodies targeting the vegf receptor-2 (flk1/kdr) as an anti-angiogenic therapeutic strategy," *Cancer Metastasis Rev.* **17**(2), 155–161 (1998).
45. Y. Xue, P. Religa, R. Cao, A. J. Hansen, F. Lucchini, B. Jones, Y. Wu, Z. Zhu, B. Pytowski, Y. Liang, W. Zhong, P. Vezzone, B. Rozell, and Y. Cao, "Anti-VEGF agents confer survival advantages to tumor-bearing mice by improving cancer-associated systemic syndrome," *Proc. Natl. Acad. Sci. U.S.A.* **105**(47), 18513–18518 (2008).
46. D. Zhang, E.-m. E. Hedlund, S. Lim, F. Chen, Y. Zhang, B. Sun, and Y. Cao, "Antiangiogenic agents significantly improve survival in tumor-bearing mice by increasing tolerance to chemotherapy-induced toxicity," *Proc. Natl. Acad. Sci. U.S.A.* **108**(10), 4117–4122 (2011).
47. G. Reyes, A. Villanueva, C. García, F. J. Sancho, J. Piulats, F. Lluís, and G. Capellá, "Orthotopic xenografts of human pancreatic carcinomas acquire genetic aberrations during dissemination in nude mice," *Cancer Res.* **56**(24), 5713–5719 (1996).
48. G. Capellá, L. Farré, A. Villanueva, G. Reyes, C. García, G. Tarafa, and F. Lluís, "Orthotopic models of human pancreatic cancer," *Ann. N.Y. Acad. Sci.* **880**(93), 103–109 (1999).
49. G. Jiménez-Valerio, M. Martínez-Lozano, N. Bassani, A. Vidal, M. Ochoa-de Olza, C. Suárez, X. García-del Muro, J. Carles, F. Viñals, M. Graupera, S. Indraccolo, and O. Casanovas, "Resistance to Antiangiogenic Therapies by Metabolic Symbiosis in Renal Cell Carcinoma PDX Models and Patients," *Cell Reports* **15**(6), 1134–1143 (2016).
50. K. Garber, "Personal mouse colonies give hope for pancreatic cancer patients," *J. Natl. Cancer Inst.* **99**(2), 105–107 (2007).
51. C. J. Bruns, M. Shrader, M. T. Harbison, C. Portera, C. C. Solorzano, K.-W. Jauch, D. J. Hicklin, R. Radinsky, and L. M. Ellis, "Effect of the vascular endothelial growth factor receptor-2 antibody DC101 plus gemcitabine on growth, metastasis and angiogenesis of human pancreatic cancer growing orthotopically in nude mice," *Int. J. Cancer.* **102**(2), 101–108 (2002).
52. R. T. Tong, Y. Boucher, S. V. Kozin, F. Winkler, D. J. Hicklin, and R. K. Jain, "Vascular normalization by vascular endothelial growth factor receptor 2 blockade induces a pressure gradient across the vasculature and improves drug penetration in tumors," *Cancer Res.* **64**(11), 3731–3736 (2004).
53. K. Vishwanath, D. Klein, K. Chang, T. Schroeder, M. W. Dewhirst, and N. Ramanujam, "Quantitative optical spectroscopy can identify long-term local tumor control in irradiated murine Head Neck xenografts," *J. Biomed. Opt.* **14**(5), 054051 (2009).
54. H. Youssofian, D. J. Hicklin, and E. K. Rowinsky, "Review: Monoclonal antibodies to the vascular endothelial growth factor receptor-2 in cancer therapy," *Clin. Cancer Res.* **13**(18), 5544–5548 (2007).
55. O. Casanovas, D. J. Hicklin, G. Bergers, and D. Hanahan, "Drug resistance by evasion of antiangiogenic targeting of VEGF signaling in late-stage pancreatic islet tumors," *Cancer Cell* **8**(4), 299–309 (2005).
56. M. Pàez-Ribes, E. Allen, J. Hudock, T. Takeda, H. Okuyama, F. Viñals, M. Inoue, G. Bergers, D. Hanahan, and O. Casanovas, "Antiangiogenic therapy elicits malignant progression of tumors to increased local invasion and distant metastasis," *Cancer Cell* **15**(3), 220–231 (2009).
57. T. M. Bydlon, R. Nachabé, N. Ramanujam, H. J. C. M. Sterenborg, and B. H. W. Hendriks, "Chromophore based analyses of steady-state diffuse reflectance spectroscopy: current status and perspectives for clinical adoption," *J. Biophotonics* **8**(1-2), 9–24 (2015).
58. P. Farzam, "Hybrid diffuse optics for monitoring of tissue hemodynamics with applications in oncology," Ph.D. thesis, ICFO-The Institute of Photonic Sciences (2014).
59. T. Durduran, R. Choe, W. B. Baker, and A. G. Yodh, "Diffuse optics for tissue monitoring and tomography," *Rep. Prog. Phys.* **73**(7), 076701 (2010).
60. G. Yu, "Near-infrared diffuse correlation spectroscopy in cancer diagnosis and therapy monitoring," *J. Biomed. Opt.* **17**(1), 010901 (2012).
61. R. C. Mesquita, T. Durduran, G. Yu, E. M. Buckley, M. N. Kim, C. Zhou, R. Choe, U. Sunar, and A. G. Yodh,

- "Direct measurement of tissue blood flow and metabolism with diffuse optics," *Philos. Trans. A Math. Phys. Eng. Sci.* **369**(1955), 4390–406 (2011).
62. R. A. Weersink, J. E. Hayward, K. R. Diamond, and M. S. Patterson, "Accuracy of Noninvasive In Vivo Measurements of Photosensitizer Uptake Based on a Diffusion Model of Reflectance Spectroscopy," *Photochem. Photobiol.* **66**(3), 326–335 (1997).
63. M. G. Nichols, E. L. Hull, and T. H. Foster, "Design and testing of a white-light, steady-state diffuse reflectance spectrometer for determination of optical properties of highly scattering systems," *Appl. Opt.* **36**(1), 93–104 (1997).
64. S. L. Jacques and B. W. Pogue, "Tutorial on diffuse light transport," *J. Biomed. Opt.* **13**(4), 041302 (2008).
65. W. G. Zijlstra, A. Buursma, and O. W. van Assendelft, *Visible and Near Infrared Absorption Spectra of Human and Animal Haemoglobin: Determination and Application* (VSP, 2000).
66. S. Takatani and M. D. Graham, "Theoretical Analysis of Diffuse Reflectance from a Two-Layer Tissue Model," *IEEE Trans. Biomed. Eng.* **BME-26**(12), 656–664 (1979).
67. L. Kou, D. Labrie, and P. Chylek, "Refractive indices of water and ice in the 0.65- to 2.5- $\mu\text{m}$  spectral range," *Appl. Opt.* **32**(19), 3531–3540 (1993).
68. D. Boas, L. Campbell, and A. Yodh, "Scattering and Imaging with Diffusing Temporal Field Correlations," *Phys. Rev. Lett.* **75**(9), 1855–1858 (1995).
69. D. Boas, S. Sakadžić, J. Selb, P. Farzam, M. Franceschini, and S. Carp, "Establishing the diffuse correlation spectroscopy signal relationship with blood flow," *Neurophotonics* **3**(3), 031412 (2016).
70. R Core Team, *R: A Language and Environment for Statistical Computing*, R Foundation for Statistical Computing, Vienna, Austria (2014).
71. M. Prewett, J. Huber, Y. Li, A. Santiago, W. O'Connor, K. King, J. Overholser, A. Hooper, B. Pytowski, L. Witte, P. Bohlen, and D. J. Hicklin, "Antivascular endothelial growth factor receptor (fetal liver kinase 1) monoclonal antibody inhibits tumor angiogenesis and growth of several mouse and human tumors," *Cancer Res.* **59**(20), 5209–5218 (1999).
72. L. Witte, D. J. Hicklin, Z. Zhu, B. Pytowski, H. Kotanides, P. Rockwell, and P. Böhlen, "Monoclonal antibodies targeting the VEGF receptor-2 (Flk1/KDR) as an anti-angiogenic therapeutic strategy," *Cancer Metastasis Rev.* **17**(2), 155–161 (1998).
73. G. Yu, T. Durduran, C. Zhou, H.-W. Wang, M. E. Putt, H. M. Saunders, C. M. Sehgal, E. Glatstein, A. G. Yodh, and T. M. Busch, "Noninvasive monitoring of murine tumor blood flow during and after photodynamic therapy provides early assessment of therapeutic efficacy," *Clin. Cancer Res.* **11**(9), 3543–52 (2005).
74. T. M. Baran, J. D. Wilson, S. Mitra, J. L. Yao, E. M. Messing, D. L. Waldman, and T. H. Foster, "Optical property measurements establish the feasibility of photodynamic therapy as a minimally invasive intervention for tumors of the kidney," *J. Biomed. Opt.* **17**(9), 0980021 (2012).
75. A. Takahashi, H. Sasaki, S. J. Kim, K. Tobisu, T. Kakizoe, T. Tsukamoto, Y. Kumamoto, T. Sugimura, and M. Terada, "Markedly increased amounts of messenger RNAs for vascular endothelial growth factor and placenta growth factor in renal cell carcinoma associated with angiogenesis," *Cancer Res.* **54**(15), 4233–4237 (1994).
76. C. Menon, G. M. Polin, I. Prabhakaran, A. Hsi, C. Cheung, J. P. Culver, J. F. Pingpank, C. S. Sehgal, A. G. Yodh, D. G. Buerk, and Others, "An integrated approach to measuring tumor oxygen status using human melanoma xenografts as a model," *Cancer Res.* **63**(21), 7232–7240 (2003).
77. H.-W. Wang, J.-K. Jiang, C.-H. Lin, J.-K. Lin, G.-J. Huang, and J.-S. Yu, "Diffuse reflectance spectroscopy detects increased hemoglobin concentration and decreased oxygenation during colon carcinogenesis from normal to malignant tumors," *Opt. Express* **17**(4), 2805–2817 (2009).
78. D. Whitaker-Menezes, U. E. Martinez-Outschoorn, N. Flomenberg, R. Birbe, A. K. Witkiewicz, A. Howell, S. Pavlides, A. Tsigos, A. Ertel, R. G. Pestell, P. Broda, C. Minetti, M. P. Lisanti, and F. Sotgia, "Hyperactivation of oxidative mitochondrial metabolism in epithelial Cancer Cells in situ," *Cell Cycle* **10**(23), 4047–4064 (2011).
79. E. L. Hull, D. L. Conover, and T. H. Foster, "Carbogen-induced changes in rat mammary tumour oxygenation reported by near infrared spectroscopy," *Br. J. Cancer* **79**(11-12), 1709–1716 (1999).
80. S. Kopetz, C. Jimenez, S.-M. Tu, and P. Sharma, "Pulmonary arteriovenous fistula in a patient with renal cell carcinoma," *The Eur. Respir. J.* **29**(4), 813–815 (2007).
81. H. Simonnet, N. Alazard, K. Pfeiffer, C. Gallou, C. Bérout, J. Demont, R. Bouvier, H. Schägger, and C. Godinot, "Low mitochondrial respiratory chain content correlates with tumor aggressiveness in renal cell carcinoma," *Carcinogenesis* **23**(5), 759–768 (2002).
82. J. H. Pinthus, K. F. Whelan, D. Gallino, J. P. Lu, and N. Rothschild, "Metabolic features of clear-cell renal cell carcinoma: Mechanisms and clinical implications," *Can. Urol. Assoc. J.* **5**(4), 274–282 (2011).
83. R. Choe, M. E. Putt, P. M. Carlile, T. Durduran, J. M. Giammarco, D. R. Busch, K. W. Jung, B. J. Czerniecki, J. Tchou, M. D. Feldman, C. Mies, M. A. Rosen, M. D. Schnall, A. DeMichele, and A. G. Yodh, "Optically measured microvascular blood flow contrast of malignant breast tumors," *PLoS ONE* **9**(6), e99683 (2014).
84. G. Ramirez, A. Proctor, K. Jung, T. Wu, S. Han, R. Adams, J. Ren, D. Byun, K. Madden, E. Brown, T. Foster, P. Farzam, T. Durduran, and R. Choe, "Chemotherapeutic drug-specific alteration of microvascular blood flow in murine breast cancer as measured by diffuse correlation spectroscopy," *Biomedical Opt. Express* **7**(9), 3610 (2016).
85. U. Sunar, S. Makonnen, C. Zhou, T. Durduran, G. Yu, H.-W. Wang, W. M. Lee, and A. G. Yodh, "Hemodynamic responses to antivascular therapy and ionizing radiation assessed by diffuse optical spectroscopies," *Opt. Express* **15**(23), 15507–15516 (2007).



86. R. C. Mesquita, S. W. Han, J. Miller, S. S. Schenkel, A. Pole, T. V. Esipova, S. a. Vinogradov, M. E. Putt, A. G. Yodh, and T. M. Busch, "Tumor blood flow differs between mouse strains: Consequences for vasoresponse to photodynamic therapy," *PLoS ONE* **7**(5), 1–10 (2012).
87. D. Rohrbach, H. Salem, M. Aksahin, and U. Sunar, "Photodynamic Therapy-Induced Microvascular Changes in a Nonmelanoma Skin Cancer Model Assessed by Photoacoustic Microscopy and Diffuse Correlation Spectroscopy," *Photonics* **3**(3), 48 (2016).
88. L. Dong, M. Kudrimoti, D. Irwin, L. Chen, S. Kumar, Y. Shang, C. Huang, E. L. Johnson, S. D. Stevens, B. J. Shelton, and G. Yu, "Diffuse optical measurements of Head Neck tumor hemodynamics for early prediction of chemoradiation therapy outcomes," *J. Biomed. Opt.* **21**(8), 085004 (2016).
89. G. Yu, T. Durduran, C. Zhou, T. C. Zhu, J. C. Finlay, T. M. Busch, S. B. Malkowicz, S. M. Hahn, and A. G. Yodh, "Real-time in situ monitoring of human prostate photodynamic therapy with diffuse light," *Photochem. Photobiol.* **82**(5), 1279–84 (2007).
90. H. W. Wechsel, K. H. Bichler, G. Feil, W. Loeser, S. Lahme, and E. Petri, "Renal cell carcinoma: relevance of angiogenetic factors," *Anticancer Res.* **19**(2C), 1537–1540 (1999).
91. J. Jacobsen, K. Grankvist, T. Rasmuson, A. Bergh, G. Landberg, and B. Ljungberg, "Expression of vascular endothelial growth factor protein in human renal cell carcinoma," *BJU Int.* **93**(3), 297–302 (2004).
92. R. K. Jain, "Normalization of Tumor Vasculature: An Emerging Concept in Antiangiogenic Therapy," *Science* **307**(5706), 58–62 (2005).
93. J. Johansson, M. Mireles, J. Morales, P. Farzam, M. Martínez, O. Casanovas, and T. Durduran, "Scanning, non-contact, hybrid broadband diffuse optical spectroscopy and diffuse correlation spectroscopy system," *Biomedical Opt. Express* **7**(2), 481 (2016).

## 1. Introduction

Angiogenesis, the formation of new blood vessels, plays an important role in the growth and spread of cancer [1–3]. In order to develop angiogenesis, tumors undergo a complex signaling process by the production of angiogenic agents, one of those is the vascular endothelial growth factor (VEGF) [4]. As expected, the inhibition of angiogenesis is emerging as a new therapeutic approach to control tumor progression [5–7].

Angiogenesis inhibitors, alone or in combination with other chemotherapies, are effective in the treatment of several tumors including renal carcinomas [8–10]. However, the effective period of these agents is often limited because of the tumor resistance mechanisms [11–15]. In therapies on human patients, early identification of non-responders is essential to personalize the treatment and to avoid the resistance phase, which results in more aggressive tumors [16].

Since anti-VEGF agents are expected to inhibit the growth of new blood vessels and starve rapidly growing tumors of necessary oxygen and blood supply, we (and others) have hypothesized that local, microvascular oxygenation and blood flow are potentially important biomarkers of therapy effects. Therefore, in order to improve the outcome of antiangiogenic therapy, a practical tool for repeated measurements of oxygenation and blood flow to detect the early changes of these biomarkers is important.

There are several methods to measure the oxygen level in tumors, but due to invasiveness, depth of measurement, and utilized contrast/radiative agents, these methods are not ideal for continuous, repeated measurements [17, 18]. For the measurement of the microvascular blood flow, there are several techniques using exogenous contrast agents (sometimes with ionizing radiation) and other noninvasive techniques [19] – all with some limitations. Modalities such as positron emission tomography, dynamic X-ray computed tomography, single-photon emission computed tomography and magnetic resonance imaging are expensive modalities with limited applicability and some safety concerns due to utilization of ionized radiation or contrast agents. Others such as Doppler ultrasound are portable and suitable for repeated measurements but are often limited to the larger vasculature [20, 21] although emerging technologies are trying to address this limitation and has been used to image small vessels in rodent brains [22, 23].

Optical methods such as laser Doppler flowmetry and laser speckle flowmetry provide two-dimensional images of the blood flow in the microvasculature with good spatial resolution ( $\approx 5$ -10  $\mu\text{m}$ ). Optical coherence tomography captures micrometer-resolution, three-dimensional images of tissue structure and blood flow [24–26]. But they are all limited by the low penetration depth

(sub millimeter) and are suitable for superficial imaging. Considering the limitations of the current techniques for repeated measurements of deep tissue oxygenation and blood flow, diffuse optical techniques have gathered significant attention in both pre-clinical and clinical studies. They have a deeper penetration depth (up to few centimeters) and the penetration depth depends on the source-detector separation [27].

During the last decade many researchers have demonstrated that diffuse optics is a promising tool to monitor the hemodynamic changes (in tumors such as breast, head and neck, and prostate) induced by cancer therapies such as neoadjuvant chemotherapy, radiation therapy and photodynamic therapy. These studies have demonstrated the potential of optical monitoring of tumor hemodynamics to predict therapeutic efficiency [28–39]. In this work, we have investigated the renal cell carcinoma (RCC), which is not generally sensitive to chemotherapy, so the therapeutic options are limited. Recent development of targeted treatments has led to an improvement in RCC treatment outcomes but eventually, all tumors become resistant to anti-VEGF therapies. This study aims to demonstrate that optics has potential for monitoring anti-VEGF therapy in RCC tumors for better understanding the anti-VEGF mechanism [40, 41] and predict the outcome. For this study, we chose to use a hybrid diffuse optics system that measures blood flow by diffuse correlation spectroscopy (DCS) in addition to tissue oxygenation and hemoglobin concentration by diffuse optical spectroscopy (DOS) in order to monitor both the supply and demand side of the hemodynamic changes during antiangiogenic therapy. In principle, this could be extended to estimate the oxygen metabolism of the tumors which may turn out to be a good biomarker [31].

We have used a murine renal cell carcinoma (RCC) model, originated from human RCC biopsies and implanted on immunosuppressed mice. RCC is a highly vascular cancer and antiangiogenic therapy is the main strategy for its treatment [42, 43]. The VEGFR2 (vascular endothelial growth factor receptor 2)-blocking antibody (DC101) [44] was applied for treatment as biological and preclinical evidence suggests that the blockage of VEGFR2 could be a promising strategy to inhibit tumor-induced angiogenesis [45, 46]. We have monitored the tumor hemodynamics before and during the therapy at regular intervals and related the results to the assessment of the therapy outcome based on biopsy results.

## 2. Materials and methods

### 2.1. Animal models and the treatment procedure

The animal research project protocols for the tumorgraft models have been evaluated and accepted by IDIBELL's animal research committee and have been registered and accepted by the "Animal Experimental Commission" from the local Catalan government and the "Comisión de Ética en Experimentación Animal" from the national Spanish government. All animals were purchased from Harlan Laboratories and were housed and maintained in laminar flow cabinets under specific pathogen-free conditions.

*Orthotopic implantation of renal cell carcinoma (RCC) tumors:* The animal models are based on orthotopic implantation of small pieces ( $2 \times 2 \times 2 \text{ mm}^3$ ) of human RCC tumor biopsies by surgical implantation onto the kidney, the original neoplastic organ, on immunosuppressed nude mice, following studies pioneered by Dr. G. Capellá [47, 48]. Our samples were renal cell carcinoma of clear cell histology (REN 28), Fuhrman grade 4/4 and pathological staging pT3pN1. Fresh surgical specimens of RCC were obtained after surgical resection from the Hospital Universitari de Bellvitge (L'Hospitalet de Llobregat, Barcelona, Spain) and placed in Dulbecco's Modified Eagle's Medium (DMEM, BioWhittaker), supplemented with 10% FBS (Fetal bovine serum), 50 units/mL penicillin, and 50  $\mu\text{g/mL}$  streptomycin sulfate. The details of tumor implantation can be found in Ref [49].

Fourteen immunosuppressed male athymic nude mice of five weeks age weighing 18–22 g were measured in this study. We have implanted a piece of a human biopsy in one mouse and let the tumor grow in that animal. The enlarged tumor of the primary mouse was then extracted

and was cut in equal pieces to be implanted in 14 animals to do this experiment (same tumor for 14 animals). To minimize the heterogeneity, tumor pieces were cut from the same region of the original tumor. The process closely mimics the procedure described in Ref. [50]. These little human tumor biopsies grow in the mice, preserving the stromal architecture. Therefore, these mouse lines preserve a stromal rich tumor structure in the growing tumors with a good resemblance to the original human tumor. Thus, these animal models allow for more relevant studies of the tumor responses to treatment than standard xenograft models. To implant the tumors, the animals were first anesthetized by isoflurane inhalation then a small midline incision was made and the kidney was exteriorized. A piece of tumor was implanted on left kidney using prolene 7-0 surgical suture. The kidney was returned to the abdominal cavity and the incision was closed with wound clips.

*Antiangiogenic treatments:* The antiangiogenic drug (DC101) used is very specific monoclonal antibody that binds and blocks mouse VEGF signaling. This antibody has the advantage of having a species-restricted activity, as it does neither recognize nor block human-VEGFR2 [51–53]. Therefore, when used in the tumorgraft models, we expect that the drug does not affect the tumor cells (of human origin) directly but rather only has an antiangiogenic effect [54]. The blocking antibody of VEGFR2 (DC101) can be obtained in large scale by purification from supernatants of the hybridoma DC101 in culture (modified from ATCC) and is used at a dose of 1 mg/animal by intraperitoneal injection as previously described [55,56]. Seven mice received the antiangiogenic therapy and the rest, control group, placebo (saline). For each mouse when the tumor volume reached  $\sim 1000 \text{ mm}^3$  the therapy was started (DC101 or placebo). Day zero is the onset of therapy (the first injection was at day zero after finishing the optical measurements). All mice were treated on the same day numbers relative to their respective starting day. The measurement days matched with the therapy days, which were every 3 or 4 days (day0, day3, day 7, day10 and so on). In all cases the animals received the therapy few hours after the optical measurements. The mice kept receiving the therapy/placebo twice per week (1 mg/animal of DC101 or 1 mg/animal of saline in 200  $\mu\text{l}$  volume) up to the time that due to the tumor size, measured by palpation, or mouse weight loss, we had to stop the measurement and sacrifice the animal. On average, the control and treated animals were sacrificed respectively  $22.7 \pm 4.6$  and  $29.4 \pm 8.6$  days after the onset of the treatment.

*Tumor extraction and histologies:* After sacrificing each mouse, the tumor was extracted for the measurement of its volume (by displacement of water in a graduated cylinder) and weight (by a digital scale), and to prepare it for histological studies. In this study, we have used a cluster of differentiation 31 (CD31) staining to measure the microvessel density (MVD) in the tumor by obtaining images of sections using an optical microscope (NIKON-801 DS-Ri1, Tokyo, Japan). To quantify CD31 staining, five hot spot fields in viable tissue zones at  $\times 400$  magnification were captured for each tumor. Quantification of staining areas was performed using an image processing program, ImageJ (National Institutes of Health, Maryland, USA), by calculating the pixels corresponding to vessel areas divided by total number of pixels in the image of the stained tissue section. The percent necrotic area was also quantified by ImageJ analysis on the digitally acquired tissue sections stained with hematoxylin and eosin (H&E) by calculating the ratio of necrotic pixels to the total number of pixels in the image.

## 2.2. Optical device and data analysis

We have combined broadband near infrared diffuse optical spectroscopy (DOS) [57] and diffuse correlation spectroscopy (DCS) in a single self-calibrated probe as described below [58].

*Broadband near infrared spectroscopy device:* A quartz tungsten halogen lamp with maximum power of 250 W (66499, Newport, CA, USA) was used as the light source. The light was coupled to a 200  $\mu\text{m}$  multimode fiber to be delivered to the tissue. The detection system consisted of a 2 dimensional spectrograph (Acton InSight-EFP (1340  $\times$  400 pixels)) and a CCD camera

(PIXIS:400B-eXcelon (Princeton Instruments)), to image the reflectance spectra from multiple detection fibers over a wide range of wavelengths simultaneously. The spectrograph contains a 150 grooves/mm grating with the central wavelength set at 800 nm covering the range of 545-1055 nm. In this study we have considered the data in the range of 610-970 nm.

*Diffuse correlation spectroscopy device:* DCS uses a single longitudinal mode laser as the source (CrystaLaser, Reno, NV, USA) at 785 nm whose coherence length is much longer than the distribution of typical photon path lengths. The laser light is delivered to the tissue through a multimode fiber with a core diameter of 200  $\mu\text{m}$  ( $NA = 0.22$ ). DCS uses single mode fibers of 5.6  $\mu\text{m}$  core diameters for light collection. Four photon counting avalanche photodiodes are used as detectors (Excelitas Technologies, Waltham, MA, USA) whose output is fed to a digital correlator (Correlator.com, New Jersey, USA) to obtain the autocorrelation functions. Details of the DCS system is discussed in various reviews [59–61].

*Optical fibers and the probe design:* In this study we have deployed two probes: main and control probe. The main probe (Fiberoptic Systems Inc., Simi Valley, California) consists of both DOS and DCS fibers. Since the DOS analysis needs calibrated intensity values, the main probe is designed to be self-calibrating, featuring a miniaturized semicircle scheme for assessing the source-detector coupling coefficients [58]. There are two DOS sources (Fig. 1), one at the center of semicircle (calibration source) and the other at in one end of diameter. All nine DOS detectors are located on the circumference of a semicircle with radius of five millimeters (Fig. 1). The source in the center of semicircle that has the same distance from all nine DOS detectors which enables the estimation of the relative coupling coefficients. All DOS source and detector fibers are multimode fibers (200  $\mu\text{m}$  core). Moreover, the main probe consists of two DCS sources (200  $\mu\text{m}$  core) and seven single-mode fibers for DCS detection, which leads to 14 source-detector pairs for DCS measurements.

We have not used all the available fibers but rather deployed six source-detector separations for both DCS and DOS ranging from 1.9 to 5.0 mm. We note that the same optode distances were used for both DOS and DCS, which allowed us to probe a similar volume with both techniques. Furthermore, a second, homemade, control probe was also utilized with a single source and detector distance (4.2 mm) for both DCS and DOS. The control probe was located on a healthy muscle to catch global hemodynamics alterations during tumor measurements.

*Measurement protocol:* The optical measurement on each animal was performed on the same day as therapy induction just few hours prior to the injection of DC101/saline. The animal was anesthetized during the measurement. The anesthesia was induced by isoflurane induction in an anesthetic chamber with a 3.5% isoflurane and oxygen mixture with a flow rate of 2 L/min. After the induction of anesthesia, which was checked by toe pinch, the animal was taken out of the chamber. Maintenance of anesthesia was administered by means of a nose-cone with 2% of isoflurane and 1 L/min oxygen flow.

Mouse body temperature was kept constant at around 37°C using a heating blanket (Homeothermic Blanket Systems- Harvard Apparatus). Core body temperature was monitored continuously during the experiment using a rectal temperature probe to automatically regulate the blanket temperature.

Each session of optical measurement started by the measurement of the shoulder muscle using the main probe. The shoulder muscle was measured at four locations on the shoulder to take into account the variation due to slight probe re-location and at each location, eleven acquisitions were made. Then, the control probe was fixed on the shoulder using a probe holder and medical adhesive tape in order to capture probable hemodynamic changes. The tumor was measured by the main probe using the second probe holder at ten locations and eleven acquisitions per location. During the tumor measurement, the control probe records the same number of acquisitions as the main probe; thus for each measurement at the main probe there was a corresponding measurement of the control probe. At the end of each measurement the shoulder measurement was repeated by



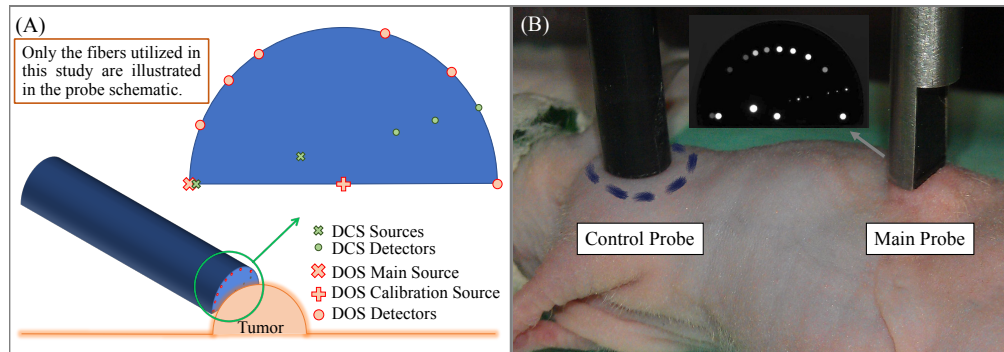


Fig. 1. (A) The schematic of hand-held DOS/DCS probe and the way it is applied on the tumor. The probe schematic only contains the location of the fibers that have been used in this study. The probe is designed to be self-calibrating, featuring a miniaturized semicircle scheme for assessing the source-detector coupling coefficients. There is a DOS source in one end of diameter and also a self-calibration source in the center of semicircle. The DOS detectors are located on the circumference of this semicircle that makes them equidistant from the calibration source. (B) An anesthetized nude mouse with a renal tumor and the optical probes (control and main) on top of the shoulder muscle and tumors with a photograph of the main probe tip on the top. Since the illuminated light to different fibers was not homogeneous they have different brightness and visibility. The smaller dots (seven locations) correspond to single mode fibers (DCS detector fibers). Not all the sources and detectors of the main probe are used in this study.

the main probe (four locations and eleven acquisitions per location) to confirm that the anesthesia has not induced considerable changes in the body hemodynamics. The location of the control probe (shoulder muscle) was roughly 5 cm away from the main probe and at this distance the light leakage between two probes was negligible. We marked a circle by a waterproof marker on a small part of shoulder to clarify the control measurement spot (Fig. 1(B)). The measurements of the shoulder were kept inside the marked area in all measurement sessions. We chose the shoulder muscle for the control site since it was an easily accessible spot with a chunk of tissue suitable for diffuse optical measurements that did not interfere with the main tumor measurement. One complete measurement session for each mouse was about thirty minutes.

### 2.3. Data analysis

**Broadband near infrared spectroscopy analysis:** The outputs of the DOS setup are the detected intensities over wavelength ( $\lambda$ ) and source-detector separation ( $\rho$ ). We go through the following procedure to obtain concentration of oxy- and deoxy-hemoglobin in *in-vivo* measurements.

At first, the the wavelength dependent dark noise of each detector was subtracted from the intensity signal obtained for both calibration ( $S_1$ ) and main source ( $S_2$ ) at each detector fiber ( $i^{th}$  detector). We call this adjusted value of measured intensity from calibration and main source  $I_m^{i1}$  and  $I_m^{i2}$  respectively. In the next step the adjusted measured intensities from the main source at all detectors,  $I_m^{i2}$ , were calibrated using the calibration factors deploying the information obtained from calibration source. To calibrate the system, we need to find the the wavelength dependent calibration factors for all detectors. We call the calibration factor of  $i^{th}$  detector and  $j^{th}$  source  $F_d^i(\lambda)$  and  $F_s^j(\lambda)$  respectively. For calibrating the detectors, we assume one detector as the reference detector and calibrate the other detectors with respect to that one. In this study, we chose to calibrate with respect to the first detector and the calibration factor of the first detector is assumed to be unity ( $F_d^1(\lambda) = 1$ ). Assuming a homogenous medium, which is the assumption in

majority of the multi-distance approaches in the field, all the detectors should represent the same intensity because they are at the distance from the calibrating source ( $I^1 = I^{11}$ ). The calibrated intensity is calculated as,  $I^1 = F_s^1(\lambda) \times F_d^i(\lambda) \times I_m^{i1}(\lambda) = F_s^1(\lambda) \times F_d^1(\lambda) \times I_m^{11}(\lambda)$ . Therefore at each detector the calibration factor can be obtained from  $F_d^i(\lambda) = \frac{I_m^{i1}(\lambda)}{I_m^{11}(\lambda)}$ . The self-calibration approach attempts to account for surface inhomogeneities (e.g. a dark spot under a detector fiber). Moreover, since we do not use a phantom for calibration, we do not need to deal with changes of coupling coefficient between phantom and tissue. Previous studies have validated the performance of the self-calibrating probe and broadband continuous wave spectroscopy [58, 62, 63].

The calibrated light intensity,  $I(\rho, \lambda)$ , at a distance  $\rho$  from the main light source is assumed to be proportional to the Green's function solution for diffusion equation in the semi-infinite boundary condition.

We have assumed a Mie-like model containing a Rayleigh term [64] for the scattering spectrum:  $A_1$  and  $A_2$ ) and reduced scattering coefficient is defined as  $\mu_s' = A_1(\frac{\lambda}{\lambda_{Reference}})^{-b} + A_2(\frac{\lambda}{\lambda_{Reference}})^{-4}$ . The measured absorption coefficients,  $\mu_a(\lambda)$ , are related to the different tissue chromophores as  $\mu_a(\lambda) = \sum_i^{nc} \epsilon_i(\lambda)c_i$ . The sum is over the different tissue chromophores. Here we have assumed only water, oxy- and deoxy-hemoglobin as chromophores ( $nc = 3$ ).  $\epsilon_i(\lambda)$  is the wavelength-dependent extinction coefficient (Molar absorption coefficient) of the  $i^{th}$  chromophore obtained from the literature: the spectrum of oxy-hemoglobin at 610-800 nm from Ref. [65] and at 800-970 nm from Ref. [66], deoxy-hemoglobin at 610-970 nm from Ref. [66], and water at 610-970 nm from Ref. [67]. Numerical fitting was done for  $A_1$ ,  $A_2$ ,  $b$  and  $c_i$  in the wavelength range 610-970 nm for the ratio of the Green's functions of two fibers at the same time,  $G(c_i, A_j, b, \rho)/G(c_i, A_j, b, \rho_0)$ . The DOS analysis relies on the comparison of the ratio of light between two different separations. This spectrum ratio becomes flatter and more difficult to fit to if the difference in source-detector separation is small. Therefore, we chose the pairs with the largest differences in source-detector separation. The three short separations (1.9, 2.5, and 2.9 mm) were used for  $\rho_0$  and the three longest (4.3, 4.6, and 5.0 mm) for  $\rho$ . The fitting was done in Matlab using a nonlinear least square method (LSQNONLIN with Levenberg-Marquardt algorithm) and the data with poor fitting quality (high residual relative to variance of the signal) were excluded.

*Diffuse correlation spectroscopy analysis:* DCS measures the temporal speckle fluctuations of the scattered light, which is sensitive to the motion of scatterers such as red blood cells which in turn could be used to estimate microvascular blood flow [59, 68, 69]. The dynamics of the medium can be determined by the measurement of the intensity autocorrelation from which the electric field autocorrelation function can be derived. The semi-infinite homogeneous medium solution to the correlation diffusion (equation 1) was employed to fit to the measured autocorrelation curves for a blood flow index (BFI) [59], given by:

$$G_1(\rho, \tau) = \frac{3\mu_s'}{4\pi} \left[ \frac{\exp(-K(\tau)r_1)}{r_1} - \frac{\exp(-K(\tau)r_b)}{r_b} \right]. \quad (1)$$

Here  $\tau$  is the delay time,  $r_1 = \sqrt{(1/\mu_s')^2 + \rho^2}$ ,  $r_b = \sqrt{(2z_b + 1/\mu_s')^2 + \rho^2}$  and  $K(\tau) = \sqrt{3\mu_a\mu_s' + 6\mu_s'^2\kappa^2\tau BFI}$ , where  $\kappa$  is the wave-number of light in the medium and  $z_b$  is the extrapolated zero boundary. In this study, for each animal, at each site of measurement (tumor or muscle), the measured  $\mu_a$  and  $\mu_s'$  at 785 nm by DOS averaged over all locations of each site (ten locations of tumor and eight locations of muscle) was introduced as inputs for DCS analysis of its corresponding site. In the fitting, the Nelder-Mead derivative-free simplex method ("fminsearch") implemented in Matlab (Mathworks, USA) was used.

#### 2.4. Statistical analysis

At each measurement session of each mouse the median and interquartile range (IQR) over all locations (ten tumor locations and eight muscle locations) and acquisitions (11 acquisitions per location) are reported. The middle line of box plots in Fig. 2 and Fig. 3 indicates the median value, the top and bottom of each box are the first and third quartile. The dashed lines (whiskers) are 1.5 times the interquartile range away from the top or bottom of the interquartile lines and any observations beyond the whisker length are marked as outliers.

The correlation between total hemoglobin concentration and blood flow index (Fig. 4) is reported by the Pearson product-moment correlation coefficient (R) using “corrcoef” function of Matlab. The same procedure is used for all reported correlations through this manuscript. In Fig. 5, the markers and error bars represent the value corresponding to average and standard deviation of measurements over all tumor locations of each mouse. The average and 95% confidence interval value of each measurement session over all mice are presented by solid black and gray lines. The fitted line is calculated by local polynomial regression fitting (“LOESS” package) with a span value fixed at 0.75 in R (open source statistical computing language [70]).

The difference between distribution of physiological parameters of muscle and tumor is investigated by a two-tailed t-test (with 95% confidence interval) employing “ttest” function of “statistics and machine learning toolbox” of Matlab.

To investigate the effect of therapy over time on the tumor volume, BFI, total hemoglobin concentration (THC), and oxygen saturation (SO<sub>2</sub>) between the first day and day eighteenth within animals, which corresponds to the period when no mouse had been sacrificed, a paired student’s t-test is deployed using “ttest” function of Matlab. Throughout this study, “p-values” less than 0.05 were considered statistically significant to reject the null hypothesis of distributions with equal means.

### 3. Results

#### 3.1. Effect of anti-VEGFR2 treatment on tumor physiology

Figure 2 demonstrates the measured microvessel density (MVD), tumor weight and percent necrotic area in treated (T1-T7) and control (C1-C7) animals after the therapy period.

Figure 2(A) shows that the median (first-third quartile) value of microvessel density (vessel count per imaging area unit) in treated animals is 24.6 (14.5- 47.0) and in controls is 62 (55.5- 75.0). Tumors of the treated mice have lower microvessel density in comparison to control group (P = 0.002).

The measured extracted tumor weight for both treated and control groups are presented in Fig. 2(B). The median value of extracted tumor weight in treated animals is 1.9 (1.5- 2.5) g and in controls is 2.7 (2.1- 3.3) g. The extracted tumors from the treated animals are lighter than control ones (P = 0.034).

Figure 2(C) shows that the percentage of necrotic area in treated and control tumors are

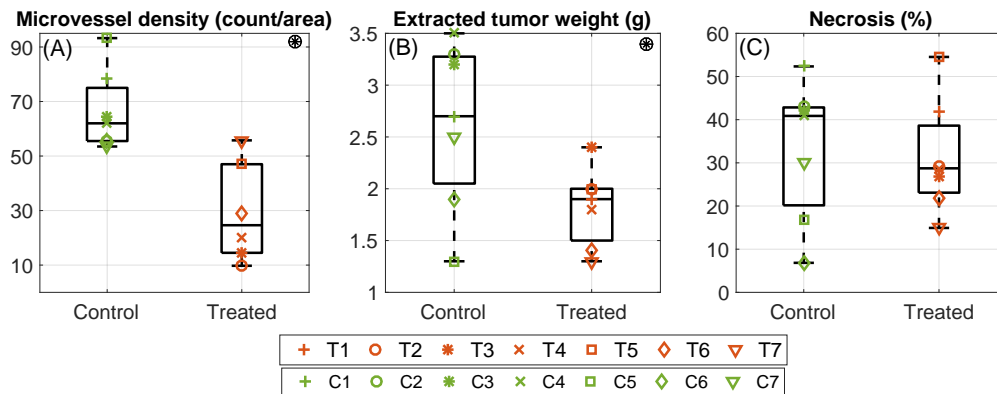


Fig. 2. The results of histologies retrieved from the extracted tumor after sacrificing the animal. T1-T7 correspond to values of seven treated animals and C1-C7 corresponds to the control animals. (A) Microvessel density (MVD) in the extracted tumor measured by CD31 staining. Tumors of treated mice have lower MVD in comparison to control group ( $P = 0.002$ ). (B) The extracted tumor weight of treated and control group. The extracted tumors from the treated animals are lighter than control ones ( $P = 0.034$ ). (C) The percentage of tumor necrotic area. There is no statistically significant difference in the tumor percent necrotic area of treated and control group ( $P = 0.8$ ). Symbol ⊗ indicates statistically significant difference between two groups (treated and control).

### 3.2. Pre-treatment optical measurements from the tumors

We have measured the wavelength dependent optical properties ( $\mu_a$  and  $\mu_s'$ ) as well as hemodynamic properties (blood oxygen saturation, total hemoglobin concentration and blood flow index) of RCC tumors and on the control site (shoulder muscle). The summary of these results is presented in table 1. For simplicity, we quote the absorption ( $\mu_a$ ) and the reduced scattering ( $\mu_s'$ ) coefficients at 785 nm since these values were utilized for the BFI calculation measured by DCS. Table 1 also shows the median and interquartile range of the repeated measurements on different locations for the pre-treatment values as a measure of tissue heterogeneity at each tissue type. In this table symbol ⊗ indicates statistically significant difference between two groups (tumor and muscle).

The comparison of the pretreatment values of hemodynamic parameters measured on the tumor and on the control (shoulder muscle) sites shows that the absorption coefficient of the tumor,  $0.19$  ( $0.17$ -  $0.21$ )  $\text{cm}^{-1}$  is lower than the muscle,  $0.25$  ( $0.24$ -  $0.27$ )  $\text{cm}^{-1}$  ( $P = 3 \times 10^{-4}$ ) but there is no significant difference between reduced scattering coefficient of tumor  $8.5$  ( $7.5$ -  $9.0$ )  $\text{cm}^{-1}$  and muscle,  $9.3$  ( $7.3$ -  $10.5$ )  $\text{cm}^{-1}$  ( $P = 0.5$ ).

As shown Fig. 3, the median of blood flow index in the tumor  $4.5$  ( $4.2$ -  $6.6$ )  $\times 10^{-8}$   $\text{cm}^2/\text{s}$  is higher than healthy shoulder muscle,  $2.3$  ( $2.2$ -  $2.6$ )  $\times 10^{-8}$   $\text{cm}^2/\text{s}$  ( $P < 10^{-4}$ ). The total hemoglobin concentration in the tumor,  $88.8$  ( $79.3$ -  $97.6$ )  $\mu\text{M}$ , is lower than the healthy shoulder muscle,  $111.6$  ( $109.3$ -  $121.0$ )  $\mu\text{M}$ , ( $P = 8 \times 10^{-4}$ ). Blood oxygen saturation of the RCC tumor is  $75.1$  ( $72.9$ -  $79.2$ )%, which is higher than healthy shoulder muscle,  $61.5$  ( $58.6$ -  $65.3$ )%, ( $P < 10^{-4}$ ).

Figure 4 shows that in both control (C1-C7) and treated (T1-T7) groups the blood flow index values (measured by DCS) and total hemoglobin concentration (measured by DOS) obtained over the course of therapy have a positive correlation (Fig. 4). The correlation coefficient for treated tumors is  $R = 0.46$  ( $P = 1 \times 10^{-4}$ ) and for control tumors is  $R = 0.44$  ( $P = 1.4 \times 10^{-4}$ ).



Table 1. Median and inter-quartile range pre-treatment (day zero) values of optically measured parameters on RCC tumors and the control muscle are shown. Furthermore, the median and inter-quartile range of variability of measured parameters in different locations is also shown to give an impression of the variability over probe re-locations at a given time point. Symbol ⊗ indicates a statistically significant difference between two tissue types (tumor and muscle)

	Tumor		Muscle	
	Median of all mice	Variability in 10 locations	Median of all mice	Variability in 8 locations
BFI (cm <sup>2</sup> /s)	⊗ 4.5 (4.2- 6.6) × 10 <sup>-8</sup>	1.1 (1.0- 1.9) × 10 <sup>-8</sup>	⊗ 2.3 (2.2- 2.6) × 10 <sup>-8</sup>	0.9 (0.6- 1.5) × 10 <sup>-8</sup>
THC (μ M)	⊗ 88.8 (79.3- 97.6)	15.2 (11.1- 18.1)	⊗ 111.6 (109.3- 121.0)	15.4 (12.8- 17.9)
SO <sub>2</sub> (%)	⊗ 75.1 (72.9- 79.2)	3.4 (2.8- 5.0)	⊗ 61.5 (58.6- 65.3)	3.2 (2.1- 3.9)
μ <sub>a</sub> (785 nm)(cm <sup>-1</sup> )	⊗ 0.19 (0.17- 0.21)	0.03 (0.02- 0.04)	⊗ 0.25 (0.24- 0.27)	0.03 (0.03- 0.04)
μ <sub>s</sub> (785 nm)(cm <sup>-1</sup> )	8.5 (7.5- 9.0)	1.4 (1.0- 2.0)	9.3 (7.3- 10.5)	2.9 (1.4- 3.3)

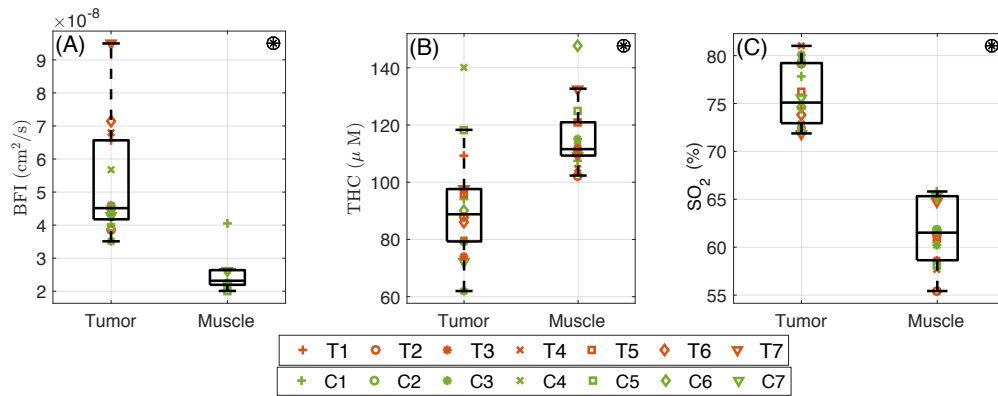


Fig. 3. The optically measured pretreatment (day zero) hemodynamic properties of the RCC tumor in comparison with the control muscle. From left to right: (A) The higher than healthy shoulder muscle value ( $P < 10^{-4}$ ). (B) The total hemoglobin concentration in the tumor is lower than the healthy shoulder muscle ( $P = 8 \times 10^{-4}$ ). (C) Blood oxygen saturation in the tumor is higher than healthy shoulder muscle ( $P < 10^{-4}$ ). Symbol ⊗ indicates statistically significant difference between two locations (tumor and muscle).

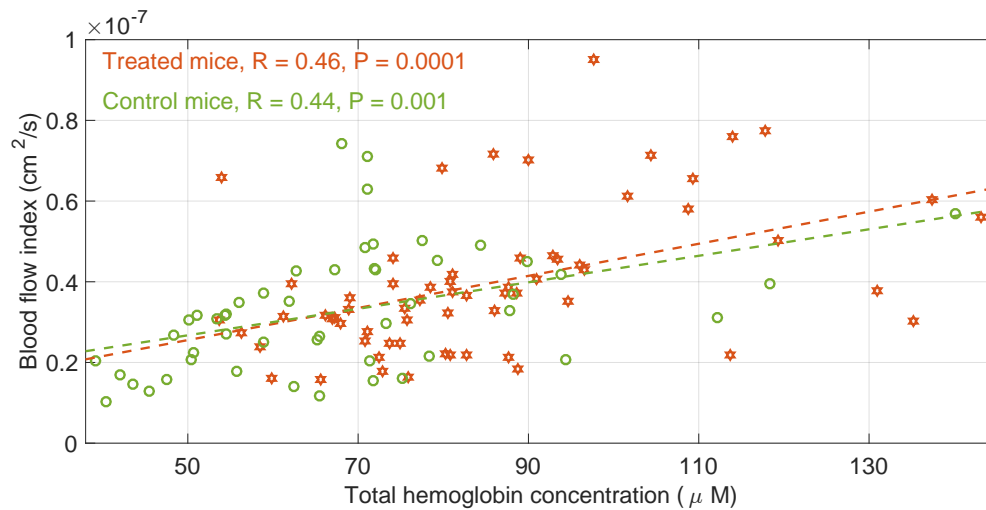


Fig. 4. The measured blood flow index versus total hemoglobin concentration measured over the course treatment on all mice. The red stars and green circles indicate measured values from treated and control animals respectively. In both control and treated group the measured total hemoglobin concentration and blood flow index have positive correlation.

### 3.3. Evolution of tumor size and hemodynamics

Figure 5 demonstrates the evolution of tumor size and optically-measured hemodynamics in treated (left column) and control (right column) tumors during the first eighteen days of therapy. The parameters were measured on the indicated days and are presented with the fitted LOESS curve and 95% confidence interval for groups of seven treated (T1-T7) and seven control animals (C1-C7). To investigate the statistical significance of changes within animals in time we have employed paired t-test between day zero and day eighteen, which corresponds to the period when no mouse had been sacrificed.

Figure 5 (subplots A and B) shows the measured tumor size by palpation during the term of therapy. The tumor size in control animals increases rapidly over time and therefore control tumors have a larger size at day eighteen compared to day zero: 200.0 (165.0- 215.0)%,  $P = 4 \times 10^{-4}$ . The therapy decelerates the tumor growth and the size of treated tumors has increased by 50.0 (25.0- 87.5)%,  $P = 0.045$ .

The blood flow index (BFI) of both treated and control animals slowly decreases as shown in Fig. 5 (subplots C and D). The change of blood flow is statistically significant for both treated and control animals ( $P = 0.025$  and  $P = 0.029$  respectively) although the change between day zero and day eighteen is smaller in control animals 4.5 (-12.4- 17.5)% versus 29.6 (20.5- 44.6)% in treated ones. Moreover, in all treated animals an initial drop of blood flow is observed during the first week of treatment. On average the blood flow in treated animals has decreased by 42 (37- 56)% after the very first session of therapy ( $P < 10^{-4}$ ) while no significant change was observed in controls.

Figure 5 (subplots E and F) shows a gradual decrease of THC in control animals with a significant change between day zero and day eighteen, 29.6 (20.5- 44.7)% ( $P = 0.02$ ), while in treated group there is no significant change in THC ( $P = 0.9$ ) and the treatment prevents the drop of THC. Finally, the blood oxygen saturation of the tumor does not have evident fluctuations in either treated or control animals, Fig. 5 (subplots G and H), although there is a slow decrease in oxygen saturation over time in control animals, 3.4 (2.2- 5.0)% ( $P = 0.042$ ). The change in treated group is statistically insignificant ( $P = 0.6$ ).

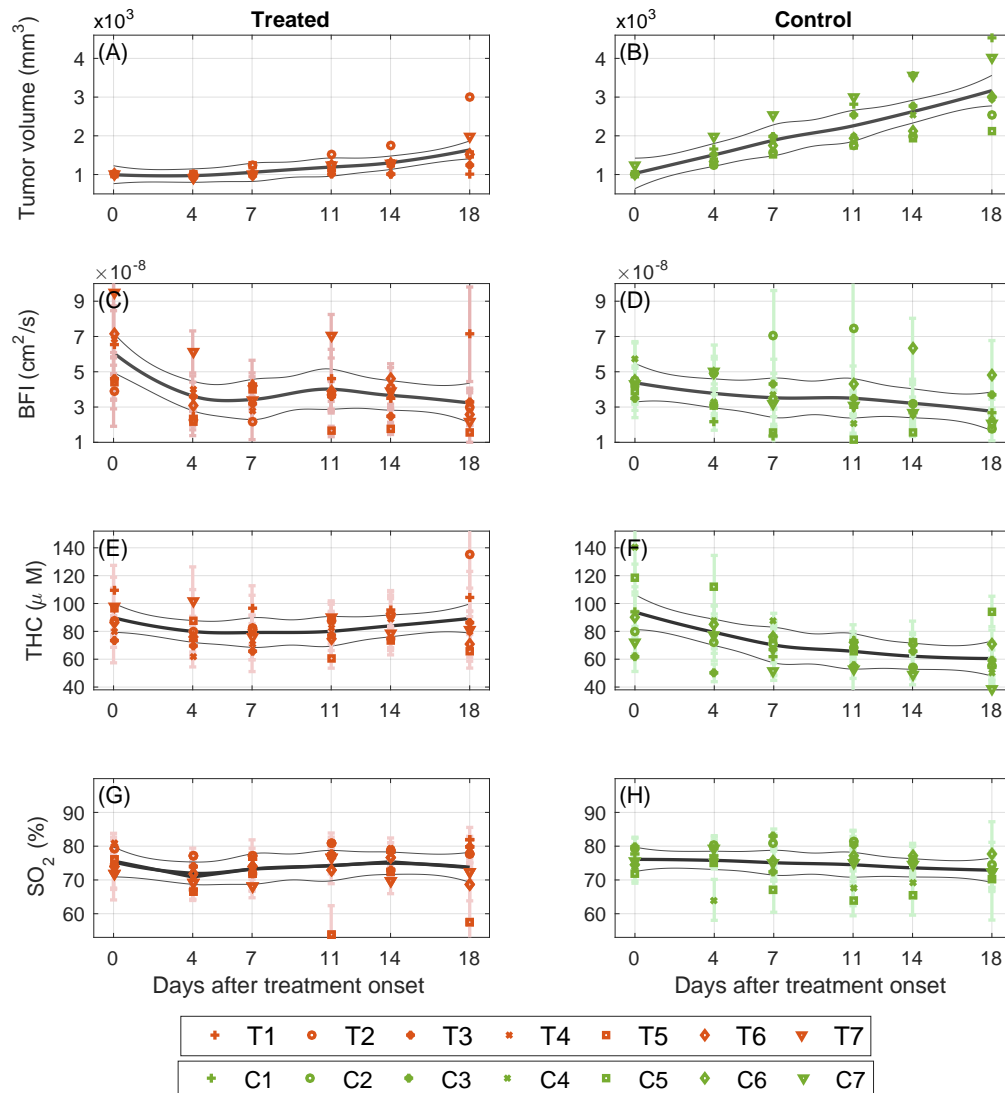


Fig. 5. Daily changes of tumor size and optically measured hemodynamic parameters during the first 18 days, which corresponds to the period when no mouse had been sacrificed, for groups of seven treated (T1-T7) in left column and seven control animals (C1-C7) in right column. Each marker and error bar represent the value corresponding to average and standard deviation of measurement over all tumor locations on a specific mouse. The solid line is a fitted LOESS curve and the gray lines are the 95% confidence intervals. (A, B) represent tumor sizes measured by palpation, (C, D) blood flow index, (E, F), total hemoglobin concentration, and (G, H) Oxygen saturation.

### 3.4. Potential biomarkers to predict the therapy outcome

As shown in Fig. 5, we have measured three hemodynamic parameters during the course of therapy and as a next step we investigate if there is a feature of them that can be an early indication of effectiveness of therapy. The antiangiogenic therapy induced significant changes as early as

four days in blood flow index ( $P = 8.9 \times 10^{-4}$ ), oxygen saturation ( $P = 0.029$ ) and borderline significance in total hemoglobin concentration ( $P = 0.051$ ).

However, not all of these indicators are consistent among all treated mice. While every individual treated tumor has shown a decrease in BFI after the first session of therapy, there is only a group change in THC and  $SO_2$ ; thus, they cannot predict individual outcome of therapy although they show a general trend. Therefore, to evaluate the capability of optically measured parameters to predict the therapeutic outcome, we have studied the correlation between BFI and conventional parameters, which are standard in oncology labs as identifiers of therapy outcome: microvessel density and tumor extracted weight. We have excluded the percentage of necrotic area since this specific therapy does not affect it (Fig. 2).

As it is presented in Fig. 6(A), there is a negative correlation between drop in BFI after the first session of therapy and the extracted tumor weight ( $R = -0.77$ ,  $P = 0.042$ ) and there is no significant correlation with the microvessel density ( $P = 0.16$ ). Since in most treated animals the drop in blood flow continues after the second session of therapy (one week) it might be more appropriate to consider the maximum blood flow drop in the first week of therapy and its relation with the therapeutic outcome. The early drop of BFI has a negative correlation with the extracted tumor weight in treated animals ( $R = -0.87$  and  $P = 0.001$ ), which suggests the tumors with larger BFI drop in the first week tend to have lighter extracted tumor Fig. 6(A). There is no significant early drop of BFI correlation and the microvessel density ( $P = 0.29$ ).

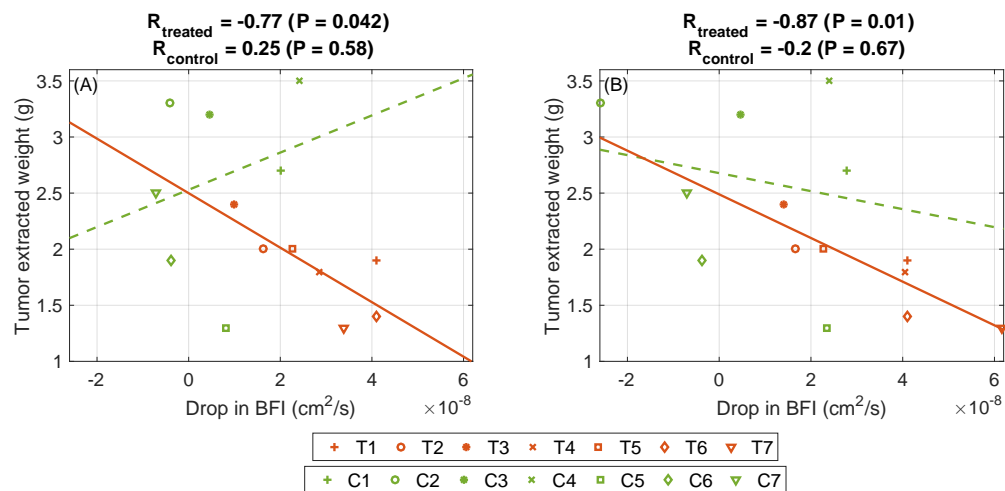


Fig. 6. The correlation between early changes of optically measured blood flow and the extracted tumor weight. (A) Correlation between drop in BFI after the first session of therapy (day four) and the extracted tumor weight. (B) The correlation between maximum BFI drop in the first week of therapy and the extracted tumor weight.

#### 4. Discussion

In this study, we have used diffuse optical techniques to monitor the changes in hemodynamics due to antiangiogenic therapy with DC101, a monoclonal antibody against mouse-VEGFR2 that is used in preclinical studies. The antibody potently blocks the binding of VEGF to its receptor, inhibited VEGF-induced signaling, and strongly blocked tumor growth in mouse tumors and human tumor xenografts through an antiangiogenic mechanism. DC101 binds with high affinity to vascular endothelial growth factor receptor 2 (VEGFR-2) and blocks the VEGF binding to the receptor in a dose-dependent manner [71, 72]. The dosage and frequency that is used in this study



is the standard dosage in this type of murine model and have the desired antiangiogenic properties that can mimic the antiangiogenic therapy in human patients. We have used several advanced mouse models of renal cell cancer (RCC), human tumorgraft RCC mouse models, designed to better resemble the human pathology [47, 48, 50]. To investigate the effect of antiangiogenic therapy in this mouse model, Fig. 2 compares the extracted tumors of treated and control group. Figure 2(A) shows that the microvessel density in the treated group, 24.6 (14.5- 47.0), is lower than controls, 62 (55.5- 75.0), and the difference is statistically significant ( $P = 0.002$ ). This result is expected since VEGF-targeted therapy blocks further new blood vessel growth.

Figure 2(B) shows that the extracted tumors from the treated animals, 1.9 (1.5- 2.5) g, are lighter than control ones, 2.7 (2.1- 3.3) g ( $P = 0.034$ ), which can be explained by considering that the VEGFR2-blocking antibody slows down the tumor growth. It is worth mentioning once more that the animals were sacrificed at different time points after the onset of therapy. The sacrificing for each animal was decided due to the tumor size threshold or mouse weight loss and weakness. In control animals the enlarged tumor was the the main reason of sacrificing the animal while in treated group with slower tumor growth they did not reach the tumor size threshold and treated animals were sacrificed due to weight loss and weakness caused by the therapy.

Figure 2(C) shows that the percentage of tumor necrotic area in treated and control tumors is respectively 28.7 (28.1- 38.6)% and 40.9 (20.2- 42.8)%. The vascular trimming in treated animals prevents tumor cells from receiving sufficient nutrition and oxygen expected to cause a larger necrotic area but we did not observe a significant difference in the tumor necrotic area of treated and control group ( $P = 0.8$ ). This might be due to two effects. First, the control mice had larger tumors when they were sacrificed, which may lead to a larger necrotic area. Second, the fact that the orthoxenograft tumors derived from a primary biopsy initially responded to DC101 antiangiogenic therapy but eventually the tumors rebounded, i.e. adapted to the treatment with DC101. When we sacrifice the animals they were in a phase of regrowth, that may be why we did not observe the expected increase in the necrotic area [11, 49].

We have applied diffuse optical methods to characterize the optical (absorption and scattering coefficients) as well as physiological properties (blood flow index, total hemoglobin concentration, and oxygen saturation) of RCC tumors and a healthy control muscle (shoulder). The source-detector separations that are utilized in this study varies between 1.9 to 5 mm. The penetration depth has direct relation with the detector distance from the source [27]. As a rule of thumb, the mean light penetration depth in the reflection geometry is in the order of one half of source-detector separation ( $\rho/2$ ), which indicates that our current probe provides information of 2-3 mm deep and allows us to reach the tissue of interest (tumor). In another study [73] with smaller optode distances (1- 3.5 mm) than our probe, the DCS measurements on superficial murine tumors under photodynamic therapy (PDT) was validated by comparison with tumor perfusion measured by power Doppler ultrasound. The two methods detected similar blood flow changes after PDT. This shows that DCS measurements have been deep enough to sense the blood flow changes in the tumor. Utilizing larger optode distances in this study ensures the sufficiency of penetration depth for monitoring of hemodynamic changes due to therapy.

The measured absorption and reduced scattering coefficients (table 1) are in good agreement with previously reported values for RCC tumors [74]. It been has reported that in RCC tumors  $\mu_s'$  (785 nm)  $\sim 8 \text{ cm}^{-1}$ , which is in agreement with our measurements:  $\mu_s' = 8.5$  (7.5- 9.0)  $\text{cm}^{-1}$ . Similarly,  $\mu_a$  (785 nm)  $\sim 0.2 \text{ cm}^{-1}$ , which is near to our reported value:  $\mu_a = 0.19$  (0.17- 0.21)  $\text{cm}^{-1}$ . Table 1 also shows the variability of measurements over different locations for the pre-treatment values as a measure of tissue heterogeneity. As expected, tissues are heterogeneous and despite this heterogeneity, we are able to detect changes between different organs and over time. It is beyond the scope of this paper to investigate the details of this variability..

As shown in Fig. 4, in both control and treated groups, total hemoglobin concentration (measured by DOS) and blood flow index (measured by DCS) have a positive correlation. The

correlation coefficients over all days for treated and control groups are respectively  $R = 0.46$  ( $P = 0.0001$ ) and  $R = 0.44$  ( $P = 0.0014$ ). The correlation shows that two independent measures by two independent devices are correlated as expected for this particular condition. Figure 3 compares the measured pre-treatment parameters in RCC tumors and a healthy control tissue (shoulder muscle). In the tumor the median of blood flow index,  $4.5 (4.2 - 6.6) \times 10^{-8} \text{ cm}^2/\text{s}$ , is higher than healthy shoulder muscle value,  $2.3 (2.2- 2.6) \times 10^{-8} \text{ cm}^2/\text{s}$  ( $P < 10^{-4}$ ) that might be due to the angiogenesis in the tumor. It is known that RCC tumors are hypervascular due to the over-expressed VEGF in them [75]. Tumors with over-expressed VEGF have an extended network of vasculature with higher measure of blood flow [76].

Malignant tumors are usually expected to be hypoxic [18, 77]. For instance, the  $\text{SO}_2$  level in murine fibrosarcoma was reported to be 36% [73]. It might be due to the enhanced mitochondrial activity [78], and, could thus, be expected to show a lower oxygen saturation. In contrast, other types of tumors due to different metabolic mechanisms experience high saturation values, for instance, mammary adenocarcinoma in rats have  $\text{SO}_2$  values about 75% [79]. In this study, we observe that the blood oxygen saturation of the RCC tumor is 75.1 (72.9- 79.2)%, which is higher than healthy shoulder muscle, 61.5 (58.6- 65.3)% ( $P < 10^{-4}$ ). One possible contribution to this is the existence of vascular shunts in RCC tumors, which are the closed arterioles passing throughout the tumor without having the chance of any oxygen exchange [80]. Furthermore, RCC tumors rely on glycolysis for their metabolism and due to reduced mitochondrial activity they do not extract much oxygen from the blood [81, 82]. The rich blood content, which delivers oxygen and low oxygen extraction would also play a part in the high oxygenation in these tumors.

Figure 5 shows the changes of tumor size and optically-measured hemodynamics over 18 days. In the first row, it is shown that the control tumors grow gradually while therapy decreases the tumor growth rate. This might be due to the trimming of vasculature in treated animals, which limits the delivery of oxygen and nutrition needed for the high rate of growth. Moreover, expression of all VEGFRs has been detected on tumor cells therefore VEGF-targeted therapy may have direct effects on tumor cells that impair tumor growth in addition to the vascular-trimming effect [6]. It has also been observed that treated tumors do not grow for one or two weeks and start to progress afterwards. This is in agreement with previous studies [12–14], where it is discussed that tumors may transform to an evasive resistance phase after an initially effective phase of antiangiogenic therapy.

We have observed a significant early reduction in blood flow due to treatment and later recovery of those parameters (Fig. 5). The observation of early response to the treatment has the potential to help us in better understanding of the short term efficiency of antiangiogenic therapy. To do so we need to design studies with larger population. We have also observed a slow decrease in blood flow over the term of therapy that might be due to tumor growth. As shown in Fig. 6(A), there is a negative correlation between drop in blood flow index after the first session of therapy and the extracted tumor weight in treated animals ( $R = -0.77$ ,  $P = 0.042$ ). It confirms the previous findings that blood flow is an important hemodynamic biomarker in cancer studies [83]. Since in most treated animals the drop in blood flow continues after the second session of therapy (one week) we have investigated the amount of maximum change in the first week of therapy and its relation with the therapeutic outcome and we observed more pronounced negative correlation between the first week drop of blood flow and the extracted tumor weight ( $R = -0.87$  and  $P = 0.01$ ), Fig. 6(B). The animals were randomly assigned to the two groups (control and treated) but showed a difference in pre-treatment hemodynamic parameters. Presumably, this is due to the small number of animals in each group. To cancel out the pre-treatment condition of tumors, if we normalize the change of blood flow with respect to the initial value by dividing the blood flow values by the pre-treatment value, the correlation between early blood flow change and final tumor weight stays in place ( $R = 0.8$ ,  $P = 0.02$ ). There is no significant correlation between early fluctuations of THC or  $\text{SO}_2$  and histology values.

These results suggest that the therapy triggers an early change in blood flow and the amount of this change is a potential predictor of therapeutic outcome. Similarly, a recent study on murine tumors [84] suggests that blood flow measured by DCS is a biomarker for therapy outcome prediction. The study shows that onset of chemotherapy induces early blood flow change, which correlates with the treatment outcome and can be used to distinguish the treated from untreated mice individually for effective treatments. Another study that measures blood flow by DCS during photodynamic therapy in mice tumors [73] shows that the rate of changes of blood flow strongly correlates with the therapy outcome. Several other studies, which deploy DCS to monitor blood flow changes induced by therapy in murine tumors, demonstrate the importance of blood flow monitoring in pre-clinical studies for better understanding the therapy mechanism and to predict the outcome [85–87]. DCS has also been applied in clinical studies, to monitor blood flow changes induced by therapy in patients with head and neck cancer [32, 88], breast cancer [28, 31], and prostate cancer [89]. Our findings on the predictive value of blood flow is coherent with several other pre-clinical and clinical studies, which suggests that tumor blood flow is a sensitive parameter to cancer therapy and DCS can measure these flow changes to provide vital information about therapy mechanism and outcome. However, the main limitation of this exploratory study is the small number of mice. In the future, to investigate the relation between the blood flow and therapy outcome and to follow individual variability in a more quantitative manner, we will increase the study population.

Figure 5(D) shows a gradual decrease of THC ( $P = 0.02$ ) in control animals while in treated group (Fig. 5(C)) there is no significant change in THC ( $P = 0.9$ ). The decrease in THC might be due to the increased VEGF levels [90, 91] that may cause bone marrow damage and the anti-VEGF treatment plays a marrow protection role [46] as shown in murine melanoma that prevents the decrease of THC in treated mice. This needs to be further elaborated in a larger study.

In Fig. 5, panels G and H show a slow decrease in oxygen saturation over time (between day zero and 18) in treated and control animals with no significant effect in treated group ( $P = 0.6$ ) and significant, 3.4 (2.2- 5.0)% ( $P = 0.042$ ), in control group. The slight decrease in  $SO_2$  might be due to fast progress of the tumor size, which is more pronounced in control animals. In these cases the vasculature network does not expand as fast as tumor size and may lead to the necrotic area with slightly lower oxygen saturation. Moreover, in treated animals the transient normalization of tumor vessels might produce a temporary enhancement in oxygen delivery [92] that compensates the effect of tumor growth. To sum up there is no significant difference in oxygen saturation values between treated and control groups ( $P = 0.42$ ) at the last day of measurement (before sacrificing). This demonstrates that although anti-VEGF agents are successful in microvessel trimming, the collective effect of the treatment does not affect the oxygen saturation in tumors. The similar necrotic area values in treated and control animals are in agreement with this observation.

Another limitation of this study is the inherent complication of the contact probe, the variations in probe pressure. This may introduce an artificial variability in the estimated hemodynamic parameters. To overcome this challenge and to increase the spatial/temporal resolution, we can deploy non-contact optical elements to scan the tumor surface [93].

To sum up, we have deployed diffuse optical spectroscopy as a noninvasive technique suitable for repeated measurements to monitor hemodynamic changes during antiangiogenic. These results demonstrate that diffuse optics is a potential tool to understand the complex mechanism of VEGFR2-targeted therapy. Furthermore, therapy induced early changes of optically measured parameters can be used as predictors of the therapy outcome for better prognosis and therapy planning.

## 5. Conclusion

In this study, we have applied diffuse optical spectroscopy methods (DOS and DCS) for monitoring the hemodynamics of murine renal cell carcinoma (RCC) tumors during antiangiogenic therapy. DCS provides information of blood flow and DOS measures tissue absorption and scattering as well as oxygen saturation and total hemoglobin concentration. We have characterized the optical and physiological properties of RCC tumors by using the complete set of data obtained from the hybrid DOS/DCS device, where high oxygen saturation in this tumor type was observed.

There is an early response to the induction of antiangiogenic therapy, which triggers a drop in blood flow after the first session of therapy. The early changes in BFI after the first and second session of therapy (after three days and one week) correlate with the extracted tumor weight. These results suggest that diffuse optics is a potential tool to understand the complex mechanism of antiangiogenic therapy for better therapy planning.

## Funding

The project was funded by Fundació Cellex Barcelona, Marie Curie IEF (FP7 MOBODICT); Ministerio de Economía y Competitividad (PHOTODEMENTIA - DPI2015-64358-C2-1-R, SAF2012-36575, RTICC RD2006-0092); l'Obra Social La Caixa (LlumMedBCN); the "Severo Ochoa" Programme for Centres of Excellence in R&D (SEV-2015-0522); ERC-FP7 (ERC-StG-281830); AGAUR-Generalitat (2014-SGR725, 2014SGR-1555); National Institutes of Health (NIH) (K99/R00-CA126187).

## Acknowledgements

The authors thank Dr. Angels Sierra for helpful discussions and the IDIBELL animal facility staff for their support.